Automatic Segmentation of Unstained Living Cells in Bright-Field Microscope Images

Marko Tscherepanow[1], Frank Zöllner[2], Matthias Hillebrand[1], and Franz Kummert[1]

[1]Applied Computer Science, Faculty of Technology,
Bielefeld University, P.O. Box 100 131, D-33501 Bielefeld, Germany
{marko,mhillebr,franz}@techfak.uni-bielefeld.de

[2]Computer Assisted Clinical Medicine, Faculty of Medicine Mannheim
University of Heidelberg, Theodor-Kutzer-Ufer 1-3
D-68167 Mannheim, Germany
frank.zoellner@medma.uni-heidelberg.de

Abstract. The automatic subcellular localisation of proteins in living cells is a critical step in determining their function. The evaluation of fluorescence images constitutes a common method of localising these proteins. For this, additional knowledge about the position of the considered cells within an image is required. In an automated system, it is advantageous to recognise these cells in bright-field microscope images taken in parallel with the regarded fluorescence micrographs. Unfortunately, currently available cell recognition methods are only of limited use within the context of protein localisation, since they frequently require microscopy techniques that enable images of higher contrast (e.g. phase contrast microscopy or additional dyes) or can only be employed with too low magnifications. Therefore, this article introduces a novel approach to the robust automatic recognition of unstained living cells in bright-field microscope images. Here, the focus is on the automatic segmentation of cells.

1 Introduction

The complete nucleotide sequences of the genomes of a variety of species have been determined in recent years. But although we have read the genetic message of these organisms, we still do not know its meaning. Based on hereditary information, macromolecules are formed, the majority of which consists of proteins. These proteins are responsible for performing numerous functions such as assembling biological structures and controlling chemical reactions. Knowledge about their functions could enable new insights into cellular processes or facilitate the development of efficient drugs.

A common approach to determining the function of proteins is the analysis of subcellular location patterns in fluorescence microscope images [1,2,3,4,5]. Based on its location within a considered cell, conclusions about a protein's function can be drawn.

P. Perner and O. Salvetti (Eds.): MDA 2008, LNAI 5108, pp. 158–172, 2008. The original publication is available at www.springerlink.com.

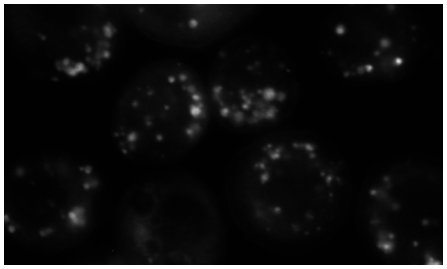

Fig. 1. Fluorescence micrograph showing Sf9 cells with stained lysosomes.

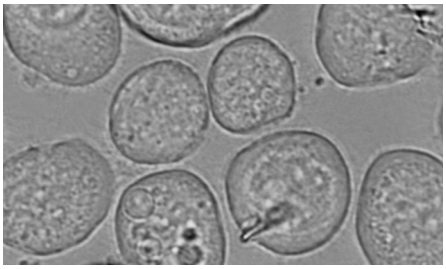

Fig. 2. Bright-field image taken simultaneously with the micrograph of Fig. 1.

In order to localise them, the considered proteins are tagged with a fluorescence dye, for instance with the green fluorescent protein (GFP) or one of its spectral variants [6]. Unfortunately, the surrounding cells themselves are almost invisible in these fluorescence images (see Fig. 1). Thus, additional information is required in order to associate fluorescent spots with specific cells. Commonly applied methods for the acquisition of this information are based on a manual segmentation [1,4] or the usage of stained cells [2,4].

In contrast, our approach enables an automatic segmentation of *Spodoptera frugiperda* cells (Sf9) without employing additional dyes. A bright-field microscope image, taken in parallel with each fluorescence image, is used for the identification of cells (see Fig. 2), which constitute the basis for the analysis of the corresponding fluorescence image.

The bright-field images are segmented by means of an active contour approach briefly outlined in [7]. After a discussion of relevant literature (see Section 2), this technique as well as required methods for the automatic determination of initial segments are described in Section 3. Section 4 proposes various enhancements that are relevant for a practical application of our approach. These methods are evaluated in Section 5. Eventually, the complete cell recognition approach is analysed and a short outlook is given in Section 6.

2 Related Work

In order to account for the limitations, which have to be considered within the context of automatic protein localisation in living cells, Section 2.1 introduces and evaluates basic microscopy techniques frequently used in conjunction with cell recognition approaches. As the choice for a recognition method strongly depends on the utilised microscopy technique, the application of several well-known approaches, which are discussed in Section 2.2, is partly impeded.

2.1 Applied Microscopy Techniques

A large number of cell recognition approaches such as [8,9,10] employ phase contrast microscopy to increase the contrast of acquired images. It visualises the

phase shift induced by the interaction of rays of light with objects varying in thickness or refractive index. Since this microscopy technique requires special objectives that reduce the amplitude of incident light, the light from fluorescent objects would be attenuated as well. An alternation of the objective between the acquisition of the images used for protein localisation and cell recognition causes further problems, since it modifies the optical path. Consequently, an association of corresponding pixels of these images would be hampered.

Besides phase contrast microscopy, numerous approaches resort to additional dyes [2,11,12,13]. If such dyes were used within the context of protein localisation, they might interfere with the examined proteins or influence the cell state.

Bright-field microscopy, i.e. the direct observation of illuminated objects, is a widely used method for cell observation. It is usually available without any special devices. But the resulting contrast is rather low, which necessitates more complex recognition techniques [14,15,16,17]. On the other hand, bright-field microscopy is compatible with fluorescence microscopy and is probably the most frequently applied microscopy technique. Therefore, we have decided to use bright-field images as the basis of our cell recognition method.

2.2 Known Approaches to Cell Recognition

The most common approach to cell recognition consists in thresholding [18,19]. But it is often applied to nuclei rather than whole cells [20,21]. As each cell usually has a single nucleus, which covers the major fraction of its volume, these tasks are roughly equivalent.

Thresholding requires a uniform and unambiguous distribution of pixel intensities, which does not occur in bright-field images that show a great variety of cell appearances. Even if fluorescence images of stained nuclei are to be analysed, fuzzy transitions between objects and the image background may result in difficulties in selecting a proper threshold. In addition, thresholding causes problems in separating adjoining objects, which have to be dealt with separately. Here for example, the distance transform and the watershed transform can be applied [20]. Nevertheless, the prior binarisation of the image leads to a loss of information, which might be crucial for the determination of the objects' exact boundaries.

As an alternative to thresholding, there are approaches that determine and link the edges of stained nuclei using geometrical constraints [12]. Unfortunately, these constraints do not necessarily reflect the shape of visible objects – especially if these objects partially overlap.

Since subcellular structures are to be analysed after cell recognition, a high magnification (60×) is required. So, the considered cells comprise about 10,000–80,000 pixels. Therefore, methods utilising small rectangular patches in order to detect whole cells (cf. [11,13,14,15]) cannot be employed, as the computational costs would be too high. So, for example, the approach proposed in [14] takes 1 to 8 minutes to recognise cells in relatively small images (640×480) using a patch size of 625 pixels on an Intel Pentium 4 processor operating at 1.6GHz.

However, Petra Perner and her co-researchers proposed a technique for recognising fungal spores using bright-field microscopy [22], which resorts to image pyramids in order to decrease the processing time. The suggested technique iteratively compares small image regions with a set of examples for the objects under consideration, referred to as cases. Since these cases constitute images themselves, the translation, rotation and scaling of the cells have to be dealt with explicitly. A more abstract representation, for instance by means of representative features, could circumvent these problems. Furthermore, it might allow for a better generalisation, since irrelevant information can be neglected. Nevertheless, the given recognition rates appear very promising.

Cells in bright-field microscope images are separated from other cells and the surrounding by their membrane. Consequently, it is beneficial to include information about it in the segmentation procedure. This can be accomplished by determining cell membrane pixels and linking them [23,24]. But, in the case of images containing numerous cells of varying shape or size, it is difficult to obtain unambiguous solutions.

As an alternative to edge-linking methods, snakes have proven advantageous [9,10]. Besides exploiting gradient and image information, they allow for the incorporation of prior knowledge on cell features such as curvature and size without assuming a rigid model. Therefore, we decided to develop a snake-based algorithm for the recognition of Sf9 cells in bright-field images [7,16]. The component of our recognition system that performs an automatic segmentation of the images is detailed in the present article.

3 Cell Segmentation in Bright-Field Images

In order to find cells in microscope images in an automated way, several tasks are fulfilled (cf. Fig. 3). First, possible cells must be localised, i.e. the positions of candidate cells are to be determined. This enables the analysis of specific image regions instead of iteratively moving a region of interest over the complete micrograph. Here, several intermediate images are computed: one image depicting the image background (see Section 3.1) and another one showing possible cell membranes (see Section 3.2). Based on these two images, small regions within the possible cells are determined – the cell markers (see Section 3.3). They reflect the positions of the surrounding cells. Unfortunately, at this step no differentiation between real cells and other image objects is possible, since not enough information about the corresponding image objects is available.

After the localisation of candidate cells, they are segmented; that is, all pixels showing a specific cell are associated with it (see Section 3.4). Then representative features describing a cell are computed and non-cell objects can be rejected. This is achieved by means of a classifier. The classification process is introduced in [16].

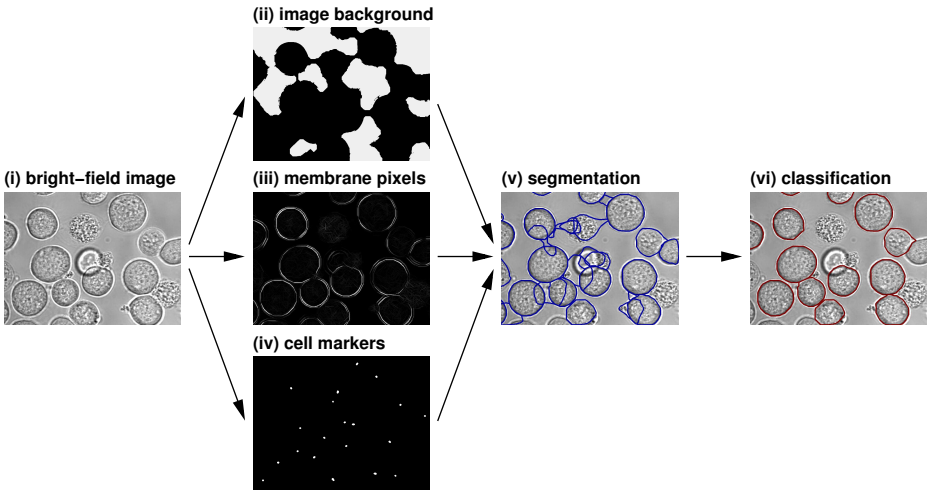

Fig. 3. Outline of the proposed cell recognition approach. On the basis of an acquired bright-field image (i) three further images which contain background pixels (ii), probable cell membrane pixels (iii) and cell markers (iv) are generated. They constitute the foundation of the proposed segmentation procedure. The segmentation (v) is followed by a classification step (vi) rejecting non-cell segments.

3.1 Separation of Image Foreground and Background

Kenong Wu and his colleagues have shown that the local intensity variation is a valuable feature for the separation of the foreground and the background in bright-field images [17]. Instead of computing the local variation defined by the variance within a square neighbourhood, we take advantage of a morphological operator: the self-complementary top-hat $\varrho_S(I)$ [25].

$$\varrho_S(I) = \phi_S(I) - \gamma_S(I) \tag{1}$$

It constitutes the difference between a closing $\phi_S(I)$ and an opening $\gamma_S(I)$, which have been applied to an image I. The required structuring element is denoted by S. This operator preserves bright as well as dark image structures that cannot include S.

Figure 4 depicts the result of the application of the self-complementary top-hat to an exemplary bright-field image as well as the corresponding variance map using a square structuring element and neighbourhood of 41×41 pixels, respectively (suggested by Wu et al.).

The bimodal distribution of the local intensity variations resulting from the application of the self-complementary top-hat is considerably more distinctive than the one computed by analysing the variance. Hence, the automatic separation of image foreground and background is alleviated. Here, minimum error thresholding [26] is utilised, as it yields excellent results for the emerging grey-level distributions [17].

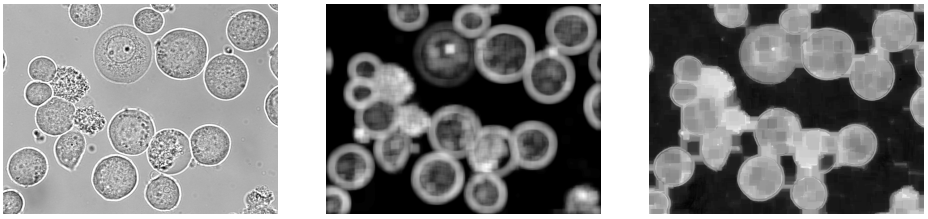

Fig. 4. Local intensity variations in a bright-field image (left). The result of the self-complementary top-hat (right) allows a noticeably better recognition of the image foreground than the variance map (centre).

In order to increase the computational efficiency, structuring elements comprising 25×25 pixels have been employed. Despite their reduced size, they still perform better than the variance map using a neighbourhood of 41×41 pixels.

In principle, the application of structuring elements that do not have a rectangular shape would be possible, as well; but, since rectangular structuring elements can be decomposed into two linear elements, they are more computationally efficient [25]. Furthermore, other shapes do not yield considerably improved results.

3.2 Detection of Probable Cell Membrane Pixels

Probable cell membrane pixels are determined by utilising morphological operators, as well, since they enable the inclusion of knowledge concerning the shape of the image structures in question. As the cell membrane possesses a linear shape that is less curved than other cell compartments, linear structuring elements are applied. The membrane is further characterised by a substantial change of intensities between neighbouring pixels. Therefore, the gradient magnitude image is utilised instead of the original image. All image structures that cannot contain the linear structuring element – e.g. dirt, noise and intracellular objects – are removed by a morphological opening. In order to get closed contours, this operation is repeated for seven additional orientations. The resulting images are fused by computing the point-wise maximum (see Fig. 5). The whole operation constitutes an algebraic opening [25].

The length l of the linear structuring elements is crucial to the result of the algebraic opening. If it is chosen too small, irrelevant image structures will remain; if the value is too high, cell membrane pixels will disappear. Hence, a procedure for the automatic determination of an optimal value had to be developed (see Section 4.1).

In order to decrease the computational effort, an optimised technique enabling the computation of morphological openings using line elements at arbitrary angles was implemented. It is based on methods proposed by Pierre Soille and his colleagues [27] who generalised an algorithm originally introduced by Marcel van Herk which solely allowed for the usage of horizontal, vertical and

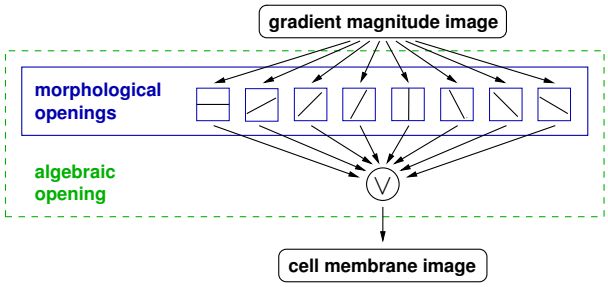

Fig. 5. Detection of pixels probably representing cell membranes. Morphological openings with linear structuring elements having eight different orientations are performed to suppress image structures that do not represent cell membranes. The resulting images are fused by a point-wise maximum operation denoted by '∨'.

diagonal lines [28]. Soille's algorithm performs morphological operations independently of the length of the linear structuring elements used. In particular, images of a specific size can be processed in constant time with respect to the structuring elements' lengths.

3.3 Determination of Cell Markers

On the basis of the computed image background and cell membrane pixels, small regions within probable cells are identified – the cell markers (see Fig. 6). It is assumed that points possessing a great distance to the image background and membrane pixels lie inside cells. These points are determined by computing the local maxima of the distance transform [25].

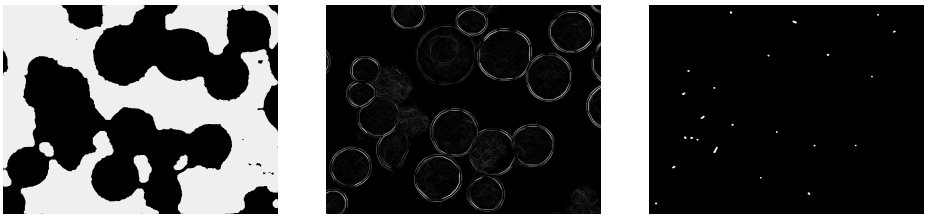

Fig. 6. Computation of cell markers. The cell markers (right) are determined in such a way that they maximise the distance to the image background (left) and membrane pixels (centre).

In order to obtain an appropriate initialisation for the segmentation step, these regions are dilated by a small circular structuring element (diameter: 5% of the maximal cell radius, 9 pixels). Afterwards, the contours are traced so as to obtain a polygonal representation that comprises only the start and the end point of adjoining lines.

3.4 Cell Segmentation by Active Contours

Active contours have several advantages with respect to the segmentation of cells. Firstly, they always yield closed contours even if the corresponding cell membrane is barely visible. Secondly, they enable the inclusion of context-specific knowledge such as membrane curvature and cell size. So, the robustness can be improved.

Several approaches have been proposed for the computation of active contours, e.g. variational calculus, dynamic programming and greedy methods. We have decided to apply a greedy approach [29] due to its efficient computability, stability and flexibility. Since our approach aims at complete independence from user interactions while processing images, special requirements have to be fulfilled. In particular, the determined cell markers instead of close approximations of the resulting contour should be applied as initialisations.

Cohen [30] proposed a method to realise the growth of snakes by introducing an inflation force. This technique resorts to normal vectors of the contour in order to determine the direction of extension. As a result, the contour might overlap with itself if it is initialised with a concave cell marker. Hence, we have decided to utilise an alternative basis for the growth of the contours – the minimal distance to the respective initial contour. Equation (2) shows the corresponding energy functional E^*_{snake} of a parametric curve $v\big(x(s), y(s)\big)$ with arc length s.

$$E^*_{\text{snake}} = \int_0^1 \big[\alpha E_{\text{cont}} + \beta E_{\text{curv}} + \gamma(E_{\text{dist}})E_{\text{ao}} + \delta(E_{\text{dist}})E_{\text{dist}}\big]ds \tag{2}$$

E_{cont} and E_{curv} control the continuity and curvature, respectively. Moreover, E_{cont} fosters equal spacing between points [29]. E_{ao} represents the resulting image of the algebraic opening (see Section 3.2) and E_{dist} the distance from the initial contour. As the energies are minimised, the image as well as the distance have to be inverted. Thus, a maximal considered distance $\Delta_{\max}$ is required. We have set it to the maximal cell radius increased by a tolerance interval of 20% (198 pixels in total).

The parameters α, β, γ and δ control the influence of the respective energy terms. Here, γ and δ are modified dependent on E_{dist}.

$$\gamma(E_{\text{dist}}) = \gamma_0 \cdot \frac{\Delta_{\max} - E_{\text{dist}}}{\Delta_{\max}} \tag{3}$$

$$\delta(E_{\text{dist}}) = \delta_0 + \gamma_0 - \gamma(E_{\text{dist}}) \tag{4}$$

According to Equation (3), $\gamma(E_{\text{dist}})$ yields high values if E_{dist} is small, i.e. if the snake has a great distance to its initialisation. By this, high pixel values near the cell markers, within the cells are suppressed. Equation (4) ensures that the sum of $\gamma(E_{\text{dist}})$ and $\delta(E_{\text{dist}})$ equals the sum of its base values γ_0 and δ_0, respectively. So, the extending force is reduced if the snake reaches a distance from its cell marker where the probability of membrane pixels is high. Additionally, background pixels receive a high value of E_{dist} in order to avoid an extension of the snake in this region.

This method allows for the snakes to be initialised by means of the cell markers, which are determined automatically and do barely resemble the final snakes. User interactions are not necessary.

4 Enhancements

In the introduction of our segmentation approach in Section 3 several questions were left open although they are crucial for the correct function. They are topics of current research and are answered in the following. Section 4.1 outlines a method that enables the automatic determination of the optimal length l for the linear structuring elements which are applied during the algebraic opening. A further problem consists in the parametrisation of the snakes. As they are growing, new points have to be inserted (see Section 4.2).

4.1 Optimal Length of the Linear Structuring Elements

The basis for the automatic determination of the length l of the linear structuring elements consists in n cell masks, which were manually extracted by biological experts. Besides the mask of a cell i itself, the points of a tube with a diameter of 5% of the mean cell radius that is centred at the mask's boundary are considered in order to detect the intensities of membrane pixels. The sets of the corresponding points p are denoted by $\mathcal{M}_i$ (mask) and $\mathcal{T}_i$ (tube), respectively. According to Equation (7), an optimal value l_{opt} for the length of the line elements is then computed by iterating over all possible values up to $\Delta_{\max}$.

$$I_l^{\mathcal{T}} = \sum_{i=1}^{n} \sum_{\forall p \in \mathcal{T}_i} I_l\big(x_p, y_p\big)^2 \tag{5}$$

$$I_l^{\mathcal{M}} = \sum_{i=1}^{n} \sum_{\forall p \in \mathcal{M}_i} I_l\big(x_p, y_p\big)^2 \Delta\big(x_p, y_p\big) \tag{6}$$

$$l_{\text{opt}} = \arg\max_{\forall l} \left(\frac{I_l^{\mathcal{T}}}{\max\limits_{\forall l} I_l^{\mathcal{T}}} - \frac{I_l^{\mathcal{M}}}{\max\limits_{\forall l} I_l^{\mathcal{M}}} \right) \tag{7}$$

$I_l\big(x_p, y_p\big)$ constitutes the image generated by an algebraic opening with a structuring element of length l. The consideration of squared pixel values results in a reduced influence of small intensities that have less negative effects on the segmentation than high ones. Moreover, the points of the mask image are weighted by their minimal distance $\Delta\big(x_p, y_p\big)$ to the boundary. l_{opt} is optimal in a sense that it maximises the difference of the intensities (scaled to fit into the interval $[0, 1]$) within both examined image regions in order to enhance the contrast.

4.2 Insertion of New Points

The segmentation consists in extending the snakes starting from small regions within probable cells. So, the distances between adjoining points are increased and a resampling of the snake, i.e. the insertion of new points is necessary. On the other hand, too high a number of points results in an increased computational effort. Thus, some kind of compromise has to be reached. Since Sf9 cells are almost elliptically shaped, an ellipse approximation of the current snake is performed [31]. This yields the lengths of the semiminor axis b and of the semimajor axis a as well as the centre C. On the basis of these values, the approximation error ϵ occurring if the ellipse is approximated by a line segment of length λ is computed (see Fig. 7).

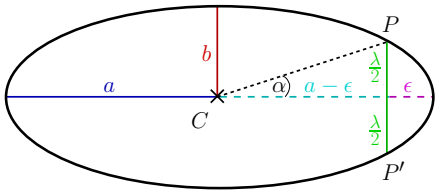

Fig. 7. Approximation of an ellipse by line segments. A line segment of length λ connecting the points P and P' causes an approximation error ϵ if it is divided equally by the major axis. As the distance between the ellipse and its centre C is maximal there, ϵ is maximal, as well. Thus, ϵ constitutes the worst case value.

An ellipse can be described by $x = a \cdot \cos\alpha$ and $y = b \cdot \sin\alpha$. Inserting the coordinates $x_P = a - \epsilon$ and $y_P = \frac{\lambda}{2}$ of point P and fusing the results leads to Equation (8) which enables the determination of λ.

$$\lambda = 2b \cdot \sin\left(\arccos\frac{a-\epsilon}{a}\right) \tag{8}$$

Instead of computing the ellipse approximation after every iteration step of the snake algorithm (variable split length, VSL), it can be applied to the determination of a constant split length λ^* (CSL). For this purpose, all manually extracted cells are approximated by an ellipse and λ^* is set to the minimal value of λ. So, a correct approximation of all cells with an error less than ϵ can be guaranteed, as well.

5 Results

We evaluated our methods on a dataset containing 499 cells manually extracted from 45 images by biological experts. In order to enable investigations regarding different foci, the dataset comprises images of the same specimens at three

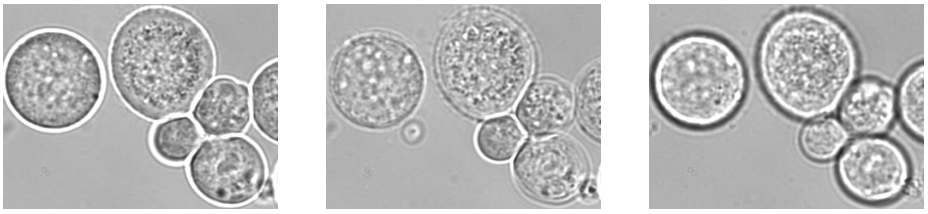

A *B* *C*

Fig. 8. Cells at different focal planes. The appearance of the examined cells varies if the focus is modified.

manually adjusted focal planes (A, B and C) showing the cell characteristics depicted in Fig. 8.

All 499 manually extracted cells were automatically marked during the preprocessing step (see Section 3.3) and each cell mask was associated with the marker closest to its centre. Furthermore, the length of the linear structuring elements for the algebraic opening was automatically set to $l_{\text{opt}} = 31$ according to Section 4.1.

In order to assess the segmentation, the manually extracted cell masks were compared with the corresponding automatically segmented cells by performing 15-fold cross-validation. The energy weights were chosen in such a way as to minimise the error term $\bar{d}^{\text{err}}$ for all except one of the images of a focal plane (see Equation (9)).

$$\bar{d}^{\text{err}} = \frac{1}{n} \sum_{i=1}^{n} \frac{d_i^{\max}}{b_i} \tag{9}$$

$d_i^{\max}$ denotes the maximal distance of corresponding manually and automatically determined contours of a cell i. These values are normed to the current manually determined cell size represented by the length of the semiminor axis b_i of the cell's approximation by an ellipse.

After computing the energy weights, the remaining image was segmented in order to measure the test errors. $\bar{d}_A^{\text{test}}$, $\bar{d}_B^{\text{test}}$ and $\bar{d}_C^{\text{test}}$ denote the mean of these test errors over all images (see Tab. 1). Additionally, the mean point number per snake $\bar{p}$ and the average processing time[1] per image $\bar{t}$ using an AMD Athlon 64 processor (2GHz) were determined.

The results of all methods show that the choice of the focal plane has a considerable effect on the quality of the segmentation. The errors rise from plane A to plane C. These results originate in less distinctive cell membranes (B) and stronger intracellular intensity variations (C), respectively (cf. Fig. 8)

Both reparametrisation methods attained smaller segmentation errors than the original approach which does not perform resampling. Since CSL utilises a minimal value of the split length λ that is sufficient for all cells, it requires additional points in comparison to VSL. These unnecessary additional points seem to deteriorate the segmentation compared to VSL (e.g. for $\epsilon = 0.125$). The

[1] excluding the time for the computation of the cell markers

Table 1. Comparison of the segmentation if variable split length (VSL), constant split length (CSL) and no resampling are applied. The dash denotes parameters that were not available.

method	ϵ	λ^*	$\bar{d}_A^{\text{test}}$	$\bar{d}_B^{\text{test}}$	$\bar{d}_C^{\text{test}}$	$\bar{p}$	$\bar{t}$
VSL	0.5	–	0.104	0.118	0.142	33.9	1.038s
	0.125	–	0.088	0.109	0.139	59.2	1.200s
CSL	0.5	18	0.094	0.130	0.143	45.2	0.802s
	0.125	9	0.102	0.116	0.141	89.6	0.980s
no resampling	–	–	0.109	0.123	0.146	23.4	0.708s

lowest errors were reached by VSL with $\epsilon = 0.125$, which required significantly more processing time than the other methods because of the determination of λ during the actual segmentation. So, if enough time is available VSL should be employed. Otherwise, the original approach and CSL, especially with $\epsilon = 0.5$, are beneficial.

In order to assess our results, the manually extracted segments of 363 cells determined by five people were compared pairwisely. The corresponding contours possess a mean maximal distance of 5% of the cell size with a standard deviation of 2.5%, as the cell membranes cannot always be determined unambiguously. Thus, we conclude that our methods are very accurate.

6 Conclusion

We have presented an approach to the automatic segmentation of cells in bright-field microscope images. Furthermore, several enhancements with respect to the quality of the preprocessing as well as the segmentation have been introduced. The result of our segmentation procedure is depicted by Fig. 9. Here, VSL with $\epsilon = 0.125$ was applied.

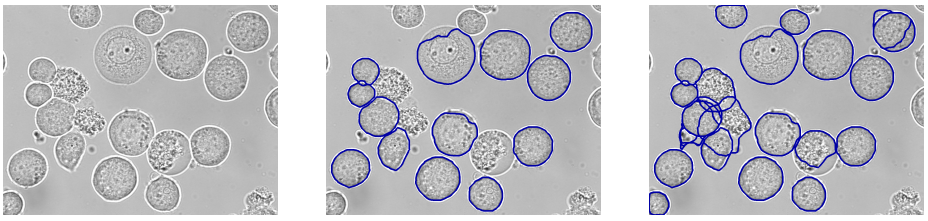

Fig. 9. Segmentation of a bright-field image (left). The final snakes are depicted as dark contours. The central image only shows segments that could be associated with manually extracted cell masks, whereas the right picture comprises all snakes.

The evaluation of our segmentation method occurred based on images at three different focal planes in order to enable the choice of an optimal one. At

this focal plane, all methods yielded excellent results insofar as the segmentation error is only slightly higher (difference $< 10\%$) than the deviations of segments manually determined by different persons.

As several cells receive multiple cell markers and other image objects – for instance dead cells and dirt – are marked as well, the number of segments is higher than the number of cells. But since the snakes are grown independently, overlapping segments do not influence one another. Furthermore, if the cell marker is situated in the centre of a real cell, the respective cell is usually segmented properly. In principle, this even enables a correct segmentation of overlapping cells. But as Sf9 cells grow adherently and the cell density is kept relatively low, the cells usually do not overlap in our images. If a cell marker does not lie close to a cell's centre, arbitrarily shaped segments might result. These segments have to be sorted out. Hence, a classification of the final snakes is performed [16]. The result of the application of our complete cell recognition approach to an independent test image is shown in Fig. 10.

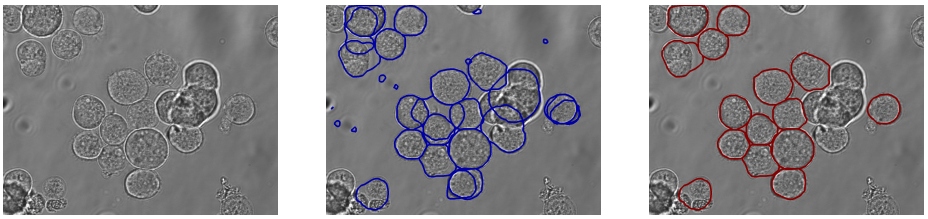

Fig. 10. Cells recognised in an independent test image (left). After the classification (right) only segments enclosing individual cells remain. Other regions yielded by the segmentation procedure (centre) are dropped.

Assuming a cell has been segmented by multiple snakes, the one best representing the cell should be chosen. Therefore, a value is computed, which reflects the confidence in the classification result [32]. Afterwards, segments that represent cells and strongly overlap are analysed and the one yielding the highest confidence value is selected.

Based on a test set comprising 302 cell masks extracted from 19 bright-field micrographs (focal planes A and B), recognition rates up to 90.1% were reached. The corresponding mean segmentation error of the recognised cells amounts to $\bar{d}^{\text{rec}}$=0.11, which confirms the results summarised by Tab. 1. The complete processing of a bright-field image (1344×1024 pixels) takes approximately 15s using an AMD Athlon 64 CPU operating at 2GHz. Although this is comparably fast, techniques such as image pyramids could probably be applied to realise a reduction of the computational load. But even without such an acceleration, this approach is suitable to be applied in conjunction with a high-throughput protein localisation technique. The first experiments regarding the usage of our cell recognition approach in conjunction with a protein localisation method have led to very promising results [5].

Recently, we have conducted experiments using an alternative cell line originating from the fruit fly *Drosophila melanogaster* [32]. Although these cells are considerably more difficult to recognise, our cell recognition method – after it had been adapted to them – performed very well.

References

1. Huh, W.K., Falvo, J.V., Gerke, L.C., Carroll, A.S., Howson, R.W., Weissman, J.S., O'Shea, E.K.: Global analysis of protein localization in budding yeast. Nature **425** (2003) 686–691
2. Liebel, U., Starkuviene, V., Erfle, H., Simpson, J.C., Poustka, A., Wiemann, S., Pepperkok, R.: A microscope-based screening platform for large-scale functional protein analysis in intact cells. FEBS Letters **554** (2003) 394–398
3. Murphy, R.F., Velliste, M., Porreca, G.: Robust numerical features for description and classification of subcellular location patterns in fluorescence microscope images. Journal of VLSI Signal Processing **35** (2003) 311–321
4. Chen, X., Murphy, R.F.: Interpretation of protein subcellular location patterns in 3D images across cell types and resolutions. In: Proceedings of the International Conference on Bioinformatics Research and Development (BIRD). Springer (2007) 328–342
5. Tscherepanow, M., Kummert, F.: Subcellular localisation of proteins in living cells using a genetic algorithm and an incremental neural network. In: Bildverarbeitung für die Medizin 2007, Springer (2007) 11–15
6. Tsien, R.Y.: The green fluorescent protein. Annual Review of Biochemistry **67** (1998) 509–544
7. Tscherepanow, M., Zöllner, F., Kummert, F.: Aktive Konturen für die robuste Lokalisation von Zellen. In: Bildverarbeitung für die Medizin 2005, Springer (2005) 375–379
8. Debeir, O., Ham, P.V., Kiss, R., Decaestecker, C.: Tracking of migrating cells under phase-contrast video microscopy with combined mean-shift processes. IEEE Transactions on Medical Imaging **24** (2005) 697–711
9. Ray, N., Acton, S.T., Ley, K.: Tracking leukocytes in vivo with shape and size constrained active contours. IEEE Transactions on Medical Imaging **21** (2002) 1222–1235
10. Zimmer, C., Labruyère, E., Meas-Yedid, V., Guillén, N., Olivo-Marin, J.C.: Segmentation and tracking of migrating cells in videomicroscopy with parametric active contours: A tool for cell-based drug testing. IEEE Transactions on Medical Imaging **21** (2002) 1212–1221
11. Nattkemper, T.W., Wersing, H., Ritter, H., Schubert, W.: A neural network architecture for automatic segmentation of fluorescence micrographs. Neurocomputing **48** (2002) 357–367
12. Raman, S., Maxwell, C.A., Barcellos-Hoff, M.H., Parvin, B.: Geometric approach to segmentation and protein localization in cell culture assays. Journal of Microscopy **225** (2007) 22–30
13. Schubert, W., Friedenberger, M., Bode, M., Philipsen, L., Ritter, H., Nattkemper, T.W.: Automatic recognition of muscle invasive T-lymphocytes expressing dipeptidyl-peptidase IV (CD26), and analysis of the associated cell surface phenotypes. Journal of Theoretical Medicine **4** (2002) 67–74

14. Long, X., Cleveland, W.L., Yao, Y.L.: Effective automatic recognition of cultured cells in bright field images using Fisher's linear discriminant preprocessing. Image and Vision Computing **23** (2005) 1203–1213
15. Long, X., Cleveland, W.L., Yao, Y.L.: Automatic detection of unstained viable cells in bright field images using a support vector machine with an improved training procedure. Computers in Biology and Medicine **6** (2006) 339–362
16. Tscherepanow, M., Zöllner, F., Kummert, F.: Classification of segmented regions in brightfield microscope images. In: Proceedings of the International Conference on Pattern Recognition (ICPR). Volume 3., IEEE (2006) 972–975
17. Wu, K., Gauthier, D., Levine, M.: Live cell image segmentation. IEEE Transactions on Biomedical Engineering **42** (1995) 1–12
18. Chen, X., Yu, C.: Application of some valid methods in cell segmentation. In: Proceedings of SPIE. Volume 4550. (2001) 340–344
19. Grobe, M., Volk, H., Münzenmayer, C., Wittenberg, T.: Segmentierung von überlappenden Zellen in Fluoreszenz- und Durchlichtaufnahmen. In: Bildverarbeitung für die Medizin 2003. (2003) 201–205
20. Malpica, N., de Solórzano, C.O., Vaquero, J.J., Santos, A., Vallcorba, I., M.García-Sagredo, J., del Pozo, F.: Applying watershed algorithms to the segmentation of clustered nuclei. Cytometry **23** (1997) 289–297
21. Walker, R.F., Jackway, P.T., Lovell, B.: Classification of cervical cell nuclei using morphological segmentation and textural feature extraction. In: Australian and New Zealand Conference on Intelligent Information Systems. (1994) 297–301
22. Perner, P., Jänichen, S., Perner, H.: Case-based object recognition for airborne fungi recognition. Artificial Intelligence in Medicine **36** (2006) 137–157
23. Alexopoulos, L.G., Erickson, G.R., Guilak, F.: A method for quantifying cell size from differential interference contrast images: validation and application to osmotically stressed chondrocytes. Journal of Microscopy **205** (2002) 125–135
24. Young, D., Gray, A.J.: Cell identification in differential interference contrast microscope images using edge detection. In: Proceedings of the 7th British Machine Vision Conference (BMVC). Volume 1., BMVA Press (1996) 133–142
25. Soille, P.: Morphological Image Analysis: Principles and Applications. Springer-Verlag New York, Inc. (2003)
26. Kittler, J., Illingworth, J.: Minimum error thresholding. Pattern Recognition **19** (1986) 41–47
27. Soille, P., Breen, E.J., Jones, R.: Recursive implementation of erosions and dilations along discrete lines at arbitrary angles. IEEE Transactions on Pattern Analysis and Machine Intelligence **18** (1996) 562–667
28. van Herk, M.: A fast algorithm for local minimum and maximum filters on rectangular and octagonal kernels. Pattern Recognition Letters **13** (1992) 517–521
29. Williams, D.J., Shah, M.: A fast algorithm for active contours and curvature estimation. Computer Vision, Graphics, and Image Processing: Image Understanding **55** (1992) 14–26
30. Cohen, L.D.: Note: On active contour models and balloons. Computer Vision, Graphics, and Image Processing: Image Understanding **53** (1991) 211–218
31. Fitzgibbon, A.W., Pilu, M., Fisher, R.B.: Direct least square fitting of ellipses. IEEE Transactions on Pattern Analysis and Machine Intelligence **21** (1999) 476–480
32. Tscherepanow, M., Jensen, N., Kummert, F.: Recognition of unstained live Drosophila cells in microscope images. In: Proceedings of the International Machine Vision and Image Processing Conference (IMVIP), IEEE (2007) 169–176